PCCP

Experimental and Computational Investigation into the Hydrodynamics and Chemical Dynamics of Laser Ablation Aluminum Plasmas

Journal:	*Physical Chemistry Chemical Physics*
Manuscript ID	CP-ART-04-2023-001586.R1
Article Type:	Paper
Date Submitted by the Author:	16-May-2023
Complete List of Authors:	Kwapis, Emily; University of Florida, Department of Materials Science and Engineering, Nuclear Engineering Program Posey, Jacob; University of Florida, Department of Mechanical and Aerospace Engineering Medici, Enrique; University of Florida, Department of Materials Science and Engineering, Nuclear Engineering Program Berg, Kira; University of Florida, Department of Agricultural and Biological Engineering Houim, Ryan; University of Florida, Department of Mechanical and Aerospace Engineering Hartig, Kyle; University of Florida, Department of Materials Science and Engineering, Nuclear Engineering Program

PCCP

ARTICLE TYPE

Cite this: DOI: 00.0000/xxxxxxxxxx

Experimental and Computational Investigation into the Hydrodynamics and Chemical Dynamics of Laser Ablation Aluminum Plasmas†

Emily H. Kwapis,[a,*] Jacob W. Posey,[b] Enrique Medici,[a] Kira Berg,[c] Ryan W. Houim,[b] and Kyle C. Hartig[a]

Received Date
Accepted Date

DOI: 00.0000/xxxxxxxxxx

Laser ablation plasma chemistry is governed by a complex interplay between hydrodynamic plasma-gas mixing processes, thermodynamics, and rapid high-temperature chemical reactions. In this work, we investigate the gas-phase oxidation chemistry of ns-laser ablation aluminum plasmas in air using optical spectroscopy combined with advanced multi-physics modeling. Experimental measurements demonstrate the formation of AlO in the plasma plume as early as 1 μs while computational results reveal that several Al_xO_y species are distributed in the periphery of the plume at even earlier times (<20 ns) in the presence of large temperature gradients and strong shockwaves. Interactions with the ablation crater during rapid plume expansion are shown to initiate vortex formation, followed by mixing dynamics that work to pull AlO into the vortices to react with gas-phase Al to form Al_2O. Oxygen and several aluminum oxides are simultaneously pulled up through the stem of the fireball, encouraging further intermixing between reacting species and enhanced molecular formation. This work concludes that chemical dynamics in laser ablation plasmas is driven by diffusion processes, concentration gradients, and plume hydrodynamics while strong shockwaves generated during laser ablation do not impede chemical reactions.

1 Introduction

Reactive plasmas generated by pulsed laser ablation resemble the explosive expansion dynamics and fireball combustion chemistry of macroscopic detonations at the laboratory scale[1–3]. Temperatures and timescales associated with the combustion chemistry of nanosecond laser ablation (LA) plasmas and aluminized high explosives have been shown to be very comparable[3]. Furthermore, LA plasmas have also been used as physicochemical surrogates for nuclear fireballs to develop reaction mechanisms and condensation pathways for nuclear fallout particle formation and debris distributions[4–6]. More generally, laser ablation plasmas are used as excitations sources with spectroscopic methods such as laser-induced breakdown spectroscopy (LIBS), where they have been implemented with spectrochemical material analyses across the scientific community including in archeology[7,8], biology and medicine[9,10], the geosciences[11,12], forensic sciences[13,14], nuclear nonproliferation[15–17], and space exploration[18,19]. These applications exploit the physics of laser ablation, where a high-powered pulsed laser is used to vaporize (i.e., ablate) a target material to produce a luminous micro-plasma. This laser-produced plasma (LPP) is then measured to generate an optical spectrum of characteristic atomic, ionic, and molecular transition lines that combine to form a fingerprint for the ablated material. The interpretation of this measured spectrum is strongly dependent on the complex and transient spatiotemporal conditions of the plasma, while the plasma response is highly sensitive to laser parameters and environmental conditions[20]. Intermixing between reactive plasma species and oxygen in the ambient atmosphere leads to the formation of oxides that alter the composition of the plasma plume, consequently introducing molecular signatures to the spectrum that may overlap with and obscure atomic signatures[21–24]. Depending on thermodynamic and atmospheric conditions, molecular formation may follow different pathways and kinetics, further complicating the spectroscopic analysis[4,25]. In an attempt to mitigate or eliminate chemical reactions, measurements are performed in inert atmospheres in a controlled-laboratory setting[26]. However, this form of environmental con-

[a] Nuclear Engineering Program, Department of Materials Science and Engineering, University of Florida, Gainesville, FL 32611, USA. E-mail: ekwapis@ufl.edu
[b] Department of Mechanical and Aerospace Engineering, University of Florida, Gainesville, FL 32611, USA.
[c] Department of Agricultural and Biological Engineering, University of Florida, Gainesville, FL 32611, USA.

† Electronic Supplementary Information (ESI) available: Additional information on the profilometer measurements, plasma temperatures calculations using PGopher, post-processing of shadowgraphic data, and reaction mechanisms and rate constants employed in the computational model are provided. See DOI: 10.1039/cXCP00000x/

trol is not always realistic in practice, such as for in-field measurements of hazardous materials at standoff distances[27] or the chemical characterization of Martian rocks[28]. Conversely, there are applications where plasma chemistry is desirable, including nanoparticle and thin film synthesis using pulsed laser deposition[29]. Therefore, understanding the effects of environmental and atmospheric conditions on chemical reaction mechanisms and kinetics in laser ablation plasmas provides important insights into the spectroscopic analysis and particle formation of reactive plasmas.

Chemical reactions are driven by favorable temperatures and collisions between reactant particles, where molecular formation in inhomogeneous laser-produced plasmas is reported to proceed in lower-temperature regions of less than 6,000 K[30,31]. Molecules with higher dissociation energies ($D_0 > 6$ eV) are reported to form at higher temperatures and in closer proximity to the plasma core while molecules with lower dissociation energies tend to form in the periphery of the expanding plume where plasma temperatures are lower[32,33]. For aluminum LPPs, AlO preferably forms at the interface between the plasma and background gas[34]. It is well-accepted knowledge that for these oxidation reactions to occur that plasma species must intermix with ambient oxygen. However, various hypotheses presented in the literature disagree on the physical processes that drive mixing and molecular formation within LPPs. Harilal *et al.* states that the external shockwave generated during laser ablation inhibits mixing between plume and ambient gas species until the shock pressure weakens to match the ambient pressure[35]. In contrast, Shabanov and Gornushkin conclude that shockwaves induce no effect on chemical reactions in laser ablation plasmas based on modeling of plume hydrodynamics[36]. They and several other independent authors instead argue that the formation of molecular species is primarily driven by both thermal and density gradients that encourage intermixing between plasma-gas species[36–38]. Wainwright *et al.* describes this mixing as a diffusion process, pulling on diffusion flame theory to estimate diffusion coefficients for oxygen across the boundary layer of the plasma plume in aluminum LPPs[34].

Experimental measurements applied to investigate the role that plume hydrodynamics contributes towards driving the chemistry of laser ablation plasmas includes various optical spectroscopy, charge collection, and imaging methods to measure species concentrations and spatial distributions. However, while these measurements provide valuable insights into the physical and chemical processes that govern laser ablation plasmas, challenges remain in characterizing the plasma's inhomogeneous properties and chemical reaction zone due to its optically thick nature, relatively small size, and fast chemistry. To address these limitations, hydrodynamic models based on numerical solutions to the Navier-Stokes or Euler's equations are often applied to predict the evolving plasma properties and expansion dynamics of LPPs in ambient gases[39–43]. In these models, laser-matter interactions and heat conduction phenomena involved in the LA process are commonly decoupled from the plume expansion models, where the plasma is instead initialized at some time subsequent to the end of the laser pulse. Radiation losses and various transport mechanisms (e.g., diffusion, viscosity) between the plasma-gas species may or may not be included. Additionally, the plasma is often assumed to be at local thermodynamic equilibrium and to behave as an ideal gas. Select numerical models also include chemical reactions for a limited collection of diatomic molecules (e.g., N_2, CN, and AlO), unanimously predicting the formation of these molecules in the plume periphery on account of lower plasma temperatures[36–38]. However, hydrodynamic processes and fluid instabilities that would yield enhanced plasma-gas intermixing, vortex formation, and increased molecular formation are not included in these models. More advanced chemistry capabilities including the formation of polyatomic molecules and condensation reactions are also largely omitted. Consequently, methods to model the turbulent chemistry and hydrodynamics of LPPs remains a current area of significant interest in the community[44]. We propose the implementation of existing high-fidelity multi-physics codes designed to model complex, coupled physicochemical processes to address this current knowledge gap in the literature.

One such multi-physics code that offers this capability is HyBurn, which has been developed to model the extreme conditions and reactive multi-phase flows of post-detonation fireballs[45,46]. The code uses Eulerian methods combined with adaptive mesh refinements, granular compaction models, turbulent mixing methodologies, and gas-phase chemical reactions to simulate phenomena such as full-scale dust explosions[47], particle-bed combustion[48], deflagration-to-detonation transitions[49], and shock-to-detonation transitions[50]. In this work, HyBurn will be employed to simulate the atmospheric mixing processes, plume hydrodynamics, and thermochemistry of aluminum LPPs. A comprehensive set of LPP measurements is provided alongside advanced computational simulations to investigate the validity of aluminum LPP models in HyBurn, which will connect phenomena observed in experimental measurements to fundamental physical and chemical processes that are readily resolved in these computational models; thus, substantially addressing the open questions and debate in the literature on the role of plume hydrodynamics on the chemistry observed in LPPs.

2 Methods

2.1 Experimental Methods

A comprehensive suite of experimental methods are applied to characterize the LPP and external shockwave generated by the LA of an aluminum metal target, as shown in Fig. 1. Nanosecond-LA is performed at atmospheric pressure in air using the fundamental wavelength of a Q-switched Nd:YAG laser (Continuum Surelite II-10 with a 7 ns pulse duration) attenuated to an energy of 25.0±0.2 mJ. A plano-convex lens ($f = 100$ mm) is used to focus the laser beam on an aluminum sputtering target (MSE Supplies, 99.9% purity), producing a crater with a diameter of 500 μm and depth of 5 μm measured using a Bruker 3D white light profilometer.

Characterization of the laser-induced plasma is performed using laser-induced breakdown spectroscopy (LIBS) and time-resolved fast-gated imaging to study the spatiotemporal evolution and vapor-phase chemistry of the plasma plume. To

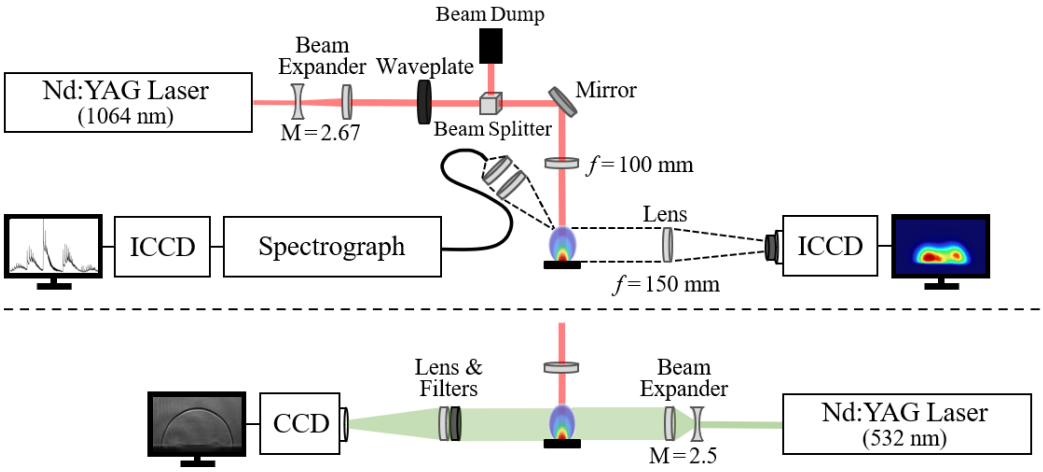

Fig. 1 Simplified experimental setups used to perform laser-induced breakdown spectroscopy, time-resolved fast-gated imaging, and shadowgraphy.

record spectroscopic signatures using LIBS, plasma emission light is collected using a pair of uncoated fused silica lenses oriented at an angle of ≈30° to the sample surface. The light is then directed into a 400 μm optical fiber that is connected to a 0.5 m focal length triple grating Czerny-Turner spectrograph (Princeton Instruments Acton SpectraPro SP-2500) and intensified emCCD camera (Princeton Instruments PI-MAX4 emICCD). Measurements are collected between 250 and 800 nm using a 1200 g/mm grating with a slit width of 40 μm, where instrumental broadening is characterized by a FWHM of 112.4 pm at 435.83 nm using a mercury calibration lamp. Due to the design of the triple grating spectrograph, 30 individual spectral windows are recorded over the full broadband wavelength range and stitched together using Princeton Instruments LightField software. Five consecutive runs for each spectral window are collected and averaged. Further intensity corrections are applied to the spectra including background subtraction and a relative instrumental response correction measured using an Ocean Insight radiometrically-calibrated deuterium-halogen lamp. Spectrally-integrated emission light is also collected separately using band-pass filters for time-resolved fast-gated imaging setup. For this setup, plasma light is collected orthogonal to the sample using a plano-convex lens ($f = 150$ mm) to focus a magnified image onto the sensor of the EMCCD camera. Two filters (394.4 nm/10 nm FWHM, 486.1 nm/10 nm FWHM) are used to image Al I and AlO emission, respectively. Five shots are averaged to produce each image.

Shock dynamics associated with the laser ablation process are captured using focused shadowgraphy. A second Nd:YAG laser is introduced to the previous setup to perform this pump-probe measurement technique, where the probe laser is frequency doubled and green light is used for imaging. To capture the external shockwave at early times (<300 ns), a machine vision lens (50 mm EFL, F/2.8) is used collect the light and focus the magnified image (M≈0.8) onto the sensor of a CCD camera (Mightex USB2.0 Monochrome CCD camera). The magnification of the setup is then decreased to M≈0.3 to image larger shockwaves at later times (>300 ns) by replacing the machine vision lens with a 100 mm focal length plano-convex lens. Beyond a time delay of 10 μs, the laser-induced shockwave is larger than the field-of-view of the camera. At this point, the pump-probe setup is again modified to better resolve the plasma plume located behind the shock front. A cuvette filled with a dilute Rhodamine 6G methanol solution is placed before the sample, where upon excitation by the 532 nm laser light the dye solution undergoes fluorescence to replace the coherent laser light as the illumination source when collecting shadowgraphic images[51]. This method was applied to remove diffraction patterns that hinder the ability to resolve the plasma flow in shadowgraphic images.

2.2 Computational Methods

Computational modeling of laser ablation aluminum plasmas is performed using the multi-physics code HyBurn. A 2D axisymmetric simulation is defined using an 8 mm x 8 mm domain with a mesh resolution of 5 μm. Slip wall and symmetry boundary conditions are assigned to the x- and y-axis, respectively. Outflow boundary conditions are defined for the upper and right domain boundaries. The simulation is initialized post-LA subsequent to the formation of the laser-produced plasma, where this plasma is initialized as a circular homogeneous aluminum fireball with a radius of 0.25 mm based on experimentally-measured shadowgraphic images recorded at a time delay of 15 ns. The initial temperature of the fireball is set to the maximum temperature (i.e., 20,000 K), while the initial pressure is set to 70 MPa based on an analysis of the shadowgraphic data; further discussion on this process will be included in the discussion on results. The fireball is placed within a 500 μm diameter crater with a depth of 50 μm, where this crater depth is defined at a larger value than the experimentally-measured crater as a consequence of the simulation mesh resolution. The atmosphere surrounding the fireball is defined as air at standard temperature and pressure. To model post-detonation chemistry, HyBurn requires inputs on thermodynamic and transport properties as well as chemical reaction mechanisms and kinetics. Thermodynamic properties for individual species are incorporated using NASA polynomials[52,53] while aluminum-oxygen reaction mechanisms and Arrhenius co-

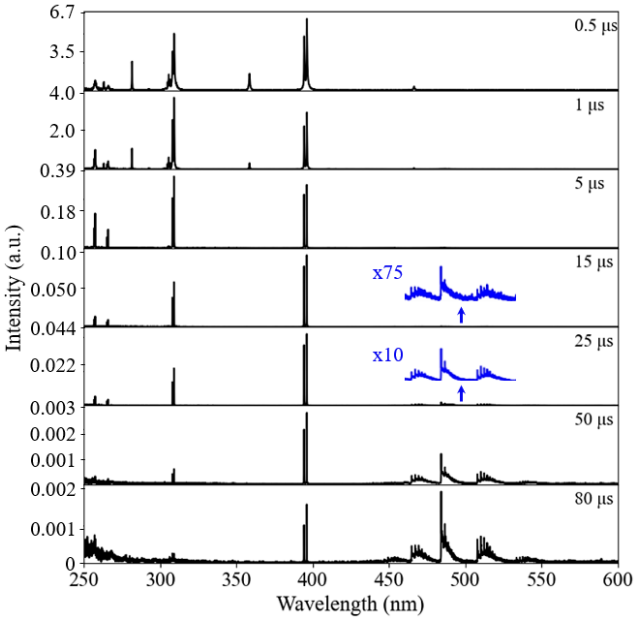

Fig. 2 Measured emission spectra of ns-LA aluminum plasmas using a laser energy of 25 mJ for various time delays.

efficients are pulled from Starik *et al.* [54] Lennard-Jones transport parameters for aluminum species are also taken from the same source [54]. Air dissociation is modeled using rate constants from Johnston and Brandis [55]. Diffusion processes are implemented as well. Real-gas effects are modeled using Becker-Kistiakowsky-Wilson (BKW) equation of state [56]. Furthermore, the HyBurn code has been verified and validated against many test problems including detonations, flames, chemical explosions, and multi-phase blasts [57–59].

Simulations are run using HiPerGator a state-of-the-art high-performance computing (HPC) resource at the University of Florida, where runtimes average around 1,200 CPU hours for the HyBurn models generated in this work. Data is post-processed and analyzed using the open-source visualization and graphical analysis software VisIt, and final plots and animations are reformatted using an in-house Python algorithm.

3 Results and Discussion

3.1 Experimental Characterization of the Laser Ablation Plasma

Aluminum LPP chemistry in air consists of oxidation reactions involving gas-phase species of aluminum and oxygen that react to form aluminum monoxide (AlO), which serves as a precursor for higher oxide states that ultimately condense and agglomerate into nanoparticles as the plasma cools. In this work, laser-induced breakdown spectroscopy is applied to monitor the early oxidation chemistry of the plasma by recording time-resolved spectroscopic signatures of Al species and AlO. From these measurements, atomic and ionic emission signals are shown to dominate at early times ($<$10 μs) while molecular signals remain weak, although the formation of AlO is first observable as early as 1 μs. AlO signal intensities do not become comparable to Al I intensities until gate delays later than 20 μs (see Fig. 2), demonstrating the time frame required for gas-phase atomic emission to decay away as electronic energy levels de-excite and the population of Al atoms is depleted through the formation of molecular species. The plasma plume temperature is also observed to decay rapidly, where this behavior is indicated by the disappearance of Al II emission within the first 5 μs of the plasma evolution. To determine the average temperature of the plasma over time, the Boltzmann plot method is implemented using the atomic transitions and spectroscopic constants provided in Table 1. As a part of this process, the spectroscopic data is also corrected for self-absorption using the semi-empirical approach presented by Sherbini *et al.* [60] Electron densities used in the calculation of the self-absorption correction factors are measured from the Hα line in the spectrum (outside range shown in Fig. 2) following the formulation derived by Oks based on advanced generalized theory [61]. The relationship between the Stark linewidth and electron density is given by Equation 1,

$$\Delta\lambda_S = 5.68\left(\frac{n_e}{10^{18}}\right)^{0.64\pm0.03} \quad (1)$$

where n_e is in cm^{-3}. Electron impact parameters for the Al I lines are tabulated as a function of temperature using values provided by Griem [62]. At later times in the plasma evolution when atomic emission is weak, plasma temperatures are estimated from the $\Delta v = -1$ band of the AlO $B^2\Sigma^+$-$X^2\Sigma^+$ transition. This is done by fitting a theoretical AlO spectrum simulated in PGopher to experimental data using molecular constants and transition strengths provided in the literature [63–67].

Overall, both the plasma temperature and electron density are observed to decay rapidly within the first 10 μs of the plasma evolution (see Fig. 3), where this behavior and comparable plasma property values are routinely reported in the literature for laser ablation aluminum plasmas [69–71]. In this work, the electron density is first measured at 300 ns with a value of $9.9{\cdot}10^{17}\pm4.9{\cdot}10^{14}$ cm^{-3} and decreases by about two orders of magnitude by 5 μs. The temperature of the plasma cools from 13,510$\pm$960 K at 1 μs to 5,570$\pm$410 K at 10 μs based on the Boltzmann plot method using self-absorption corrected Al I emission lines. A very comparable plasma temperature of 5,890$\pm$230 K is also reported at 10 μs using the AlO band, demonstrating an

Table 1 Al I transitions used to calculate plasma temperatures based on the Boltzmann plot method using spectroscopic parameters taken from the Kurucz database [68].

Wavelength (nm)	A_{ji} (10^8 s^{-1})	E_j (eV)	g_j
256.80	0.220	4.827	4
257.51	0.266	4.827	6
265.25	0.134	4.673	2
266.04	0.265	4.673	2
305.01	0.322	7.668	6
305.71	0.751	7.668	6
308.22	0.627	4.021	4
309.27	0.756	4.022	6
394.40	0.511	3.143	2
396.15	1.001	3.143	2

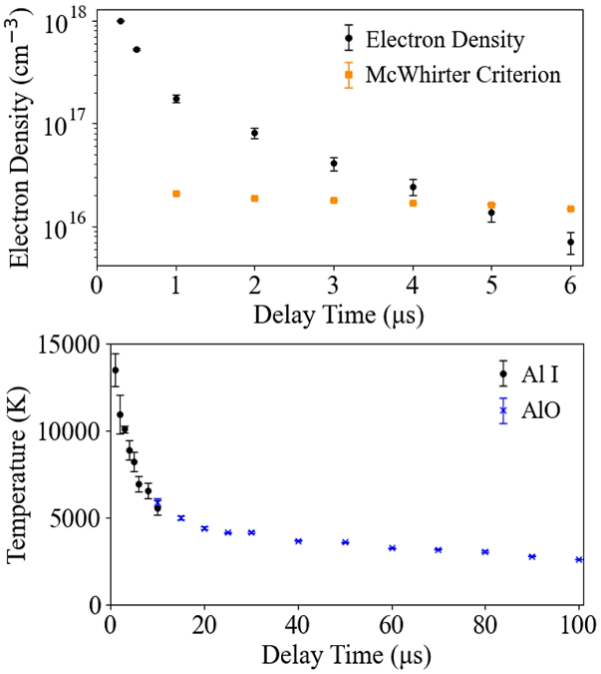

Fig. 3 Time-resolved electron densities and plasma temperatures characterizing the LA aluminum plasma.

overlap between atomic and molecular temperatures. By this time delay, the plasma does not exist at local thermodynamic equilibrium because the McWhirter criterion is not satisfied (see Fig. 3), hence, this agreement between atomic and molecular temperatures may instead be an indication that atomic and molecular species are emitting from similar locations in the LPP as compared to the existence of equilibrium conditions.

In addition to the time-resolved characterization of the aluminum plasma, spatially-resolved images of the plasma emission are collected using time-resolved fast-gated imaging to provide insights into the hydrodynamical processes and spatial distribution of chemical reaction zones of the plasma. Figure 4 demonstrates the early-time and rapid expansion of a roughly hemispherical plasma that evolves into a torus structure, demonstrated by vortex formation around 3 μs. Al I emission then collapses back into a singular structure by 8 μs, and the vortices are no longer visible. Imaging of AlO emission is first performed at 10 μs, where molecular emission is predominantly observed towards the surface of the sample. This same plume morphology was observed by Harilal *et al.* for similar experimental conditions[35]. As the plasma evolves, AlO emission is observed to move inwards towards the stem and core of the plasma plume. By 40 μs, Al I and AlO emission overlap and share very similar spatial structures, indicating probable intermixing between atomic and molecular species.

3.2 Laser Ablation Shock Dynamics

The expansion dynamics of laser-induced shockwaves generated during laser ablation carry important information on the initial blast energy and target material properties involved in the micro-explosion. Blast waves rapidly expand outward ahead of the

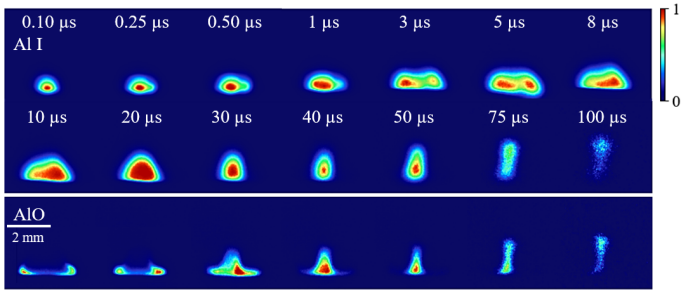

Fig. 4 Spatiotemporal distribution of Al I and AlO plasma plume species. Each individual image is normalized to its maximum intensity.

LPP, compressing and heating the ambient air to form a shock-heated gas layer between the plasma plume and shock front. Plasma species intermix with shock-heated air, ultimately leading to chemical reactions and the formation of aluminum oxides. An estimation of the thermodynamic properties of this shock-heated gas layer can be determined by applying theory on gas-dynamics to measurements of the laser-induced shockwave[72,73]. In this work, theory is combined with experimental measurements of the shock front position to determine an initial pressure for the laser ablation aluminum plasma to initialize the computational model as well as to compare and validate the numerical predictions to real data.

Focused shadowgraphy is performed to image the laser-induced shockwave from a time delay of 15 ns out to delays later than 10 μs. The shock front expansion trajectory is then extracted from the time-resolved shadowgraphic images, and shock expansion models based on a power law dependence are fitted to this trajectory to establish a semi-empirical curve for the radius of the shockwave as a function of time. The propagation velocity of the shockwave is calculated from the derivative of this curve, yielding a velocity of 8250$\pm$180 m/s at 15 ns. This velocity curve is then input into the Rankine-Hugoniot relations for an inert shock using variable specific heat to estimate the temperature and pressure of the shock-heated flow behind the shock front, yielding values of 20,800$\pm$800 K and 73.5$\pm$3.3 MPa at 15 ns. It should be acknowledged that the temperature and pressure of the shock-heated air are not necessarily equivalent to the properties of the plasma plume, however, the shockwave and fireball are initially defined with the same properties in the computational model. Based on the Rankine-Hugoniot values determined using measured data on the laser-induced shockwave, these initial simulation parameters are set to 20,000 K (i.e., maximum simulation temperature) and 70 MPa.

The shock dynamics and associated properties predicted by computational model given these initial conditions is then compared and validated against the experimentally-measured data. The shock front expansion trajectory is investigated first, where the simulation is observed to predict smaller shock front distances at early times ($<$1 μs) compared to measured data, while the opposite behavior occurs for later times (see Fig. 5). Correspondingly, the simulated shockwave velocity is initially lower than the measured propagation velocity while this behavior reverses around 300 ns. Differences between the propagation and atten-

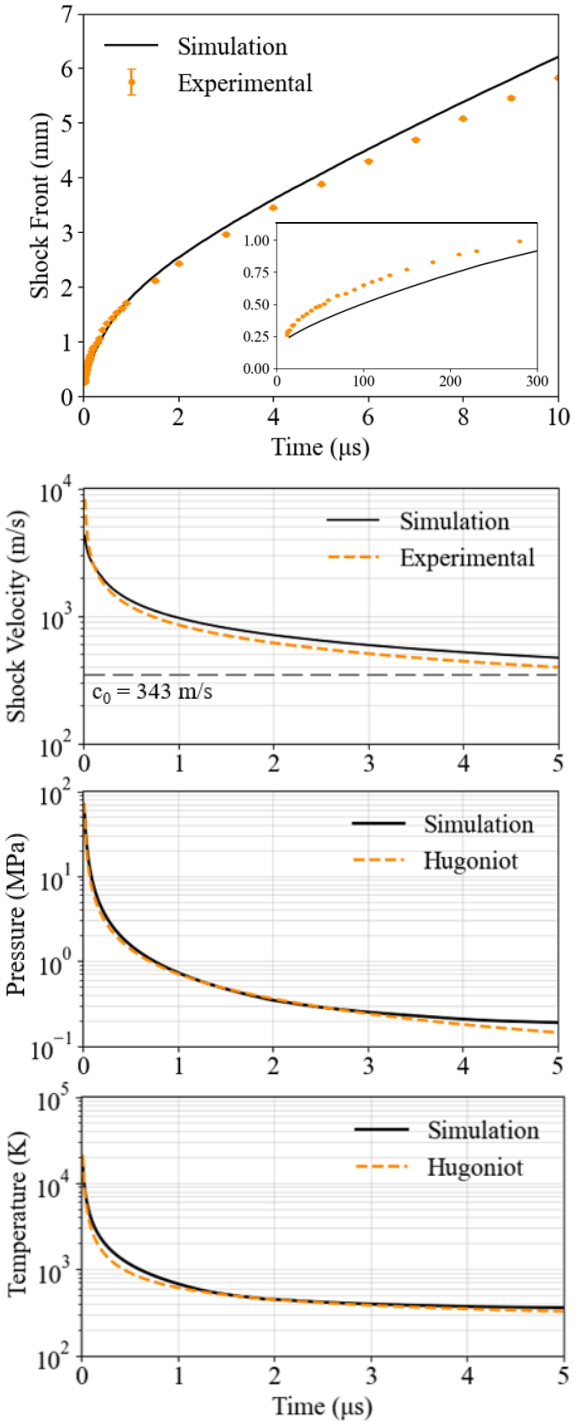

Fig. 5 Comparison of experimentally-measured and simulated properties for the shock front position, shockwave velocity, and shock-heated air properties. The Hugoniot curves are determined using experimental data.

uation of the experimental and simulated shockwaves are likely tied to assumptions made during the initialization of the shock in the computational model, which encompasses properties such as the initial energy density and crater dimensions. Moreover, the current model neglects ionization processes and radiative heat losses that may also contribute to deviations.

Additional comparisons between the experimental and computational results include the observation that both the experimentally-measured and simulated shockwave transition to an acoustic wave at times later than 5 μs when the shock velocity matches the speed of sound for air (343 m/s). The temperature and pressure of shock-heated air are also compared, where these results are shown in Fig. 5. Both properties are shown to be very comparable for the first 5 μs of the shockwave propagation, where later times are not compared because the Rankine-Hugoniot relations are only valid for shockwaves (i.e., $M_0 > 1$) and not applicable to acoustic waves. These results support the conclusion that the computational model provides informative simulations on the shock physics component of laser ablation plasmas.

Beyond the validation of the shock physics modeled by HyBurn, a visual comparison between shadowgraphs and simulated Schlieren images of the Al LPP is also provided. Figure 6 displays the close agreement in shockwave dimensions between the experimental and computational data, which was discussed earlier in this section in reference to Fig. 5. A second shockwave is also observed at a time delay of 30 μs for the shadowgraphy measurements, and is believed to represent an internal shockwave that has been reflected off of the target surface. This phenomena has been observed by others in the literature[74], and is explained to originate as a requirement to satisfy the continuity conditions during the supersonic expansion of a plasma plume against an ambient gas and associated formation of a strong outward-moving external shockwave[75,76]. During this process, an internal “return" shock is generated during the negative phase of the blast that travels in the opposite direction back towards target[77]. Upon contact with the target surface, the internal shockwave is partitioned between a stress wave that continues to propagate through the solid target material and a second shockwave that is reflected back through the plasma plume[74–76]. Arnold *et al.* and Wen *et al.* analytically model the repeated reflection of the internal shockwave between the target surface and plume front until the shock weakens and is considered negligible by 100 ns. However, experimentally reflected shocks have been reported out to times later than 20 μs in this work as well as by J.L. Gottfried[74].

Now to shift the focus away from shockwaves, attention is directed to a second hemispherical feature that is faintly observed behind the shock front in the shadowgraphs during times $\leq$1 μs (see Fig. 6). For experimental measurements this feature indicates the ionization front, which is believed be located ahead of the contact front that marks the periphery of the plasma plume[78]. Ionization processes are not modeled in this work, and hence, an ionization front is not present in the simulated images. Instead, the smaller hemisphere observed in the Schlieren images corresponds to the dissociation of air and formation of NO. The periphery of the fireball is consistently located approximately 50 μm behind the NO layer throughout the simulation. The plasma plume

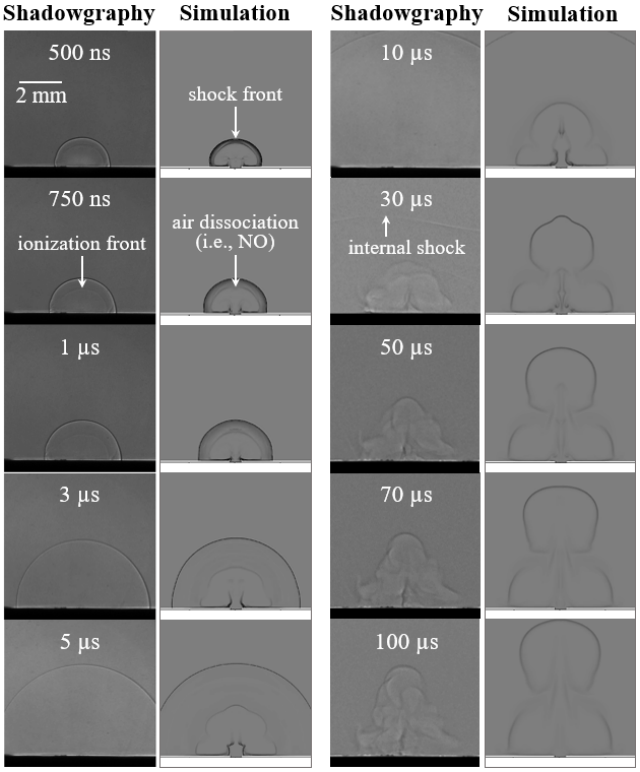

Fig. 6 Shadowgraphic measurement of the laser-induced shockwave and aluminum plasma plume compared to simulated Schlieren images.

(or fireball) periphery is resolved and imaged experimentally for later times ($\geq$30 μs), where the simulated fireball is observed to be conspicuously larger than the measured plasma during this time frame although their overall shapes remain comparable. Possible reasons for this disagreement along the axial dimension include the absence of ionization and radiative processes in the multi-physics model, as well as assumptions made when defining the initial mass and energy of the fireball. In addition, laser drilling experiments have demonstrated that deeper craters alter the shape and size of the plasma plume.[79] Because the most shallow crater that could be simulated was an order of magnitude larger than the experimental crater, this effect may also contribute to differences in plume lengths.

3.3 Modeling of Multi-Phase Plume Thermochemistry

Plume hydrodynamics and plasma-gas mixing processes involved in the multi-phase oxidation chemistry of laser ablation plasmas are modeled. Temperature distributions characterizing the fireball are provided first in Figure 7, demonstrating rapid cooling from an initial temperature of 20,000 K to around 4500 K with the first microsecond. Temperatures are heterogeneous for these early times, where hot spots are observed along the walls of the crater at 150 ns before combining into a single structure that moves upwards through the stem of the fireball at 600 ns. By a time delay of 1 μs, the average simulated plume temperature is around 4500 K. This value contrasts with the experimentally-measured temperature of about 13,500 K at the same delay time, where these underestimates on the plasma temperature may be attributed to larger fireball dimensions and kinetic plasma processes that are not included in the computational model. Despite this discrepancy, spatial distributions of the fireball temperature are believed to be representative of the laser-produced plasma properties. Large temperature gradients are generally reported at the periphery of the fireball while an outer shell of shock-heated air visibly surrounds the fireball for the first 5 μs of the simulation, which is indicated by the lighter blue hemisphere ahead of the fireball. The edge of this hemisphere marks the position of the shock front, and becomes less defined as time progresses and shock-heated temperatures decrease due to the attenuation and deceleration of the shockwave. By a time delay of 10 μs, the temperature distribution of the fireball is relatively uniform, supporting the agreement between atomic and molecular temperatures obtained by experimental measurements. Other features observed in the simulation, such as the tendrils attached to the fireball stem between 2-20 μs, are believed to represent physical phenomena and are attributed to the stem being pulled apart during the rapid fireball expansion dynamics.

Chemical reaction zones and mixing between reactive species are also investigated in addition to temperature distributions to further explain the chemical dynamics of laser ablation plasmas. Time-resolved mass fraction morphologies are provided in Figure 8, where gas-phase atomic aluminum is initially the main constituent of the fireball based on initial parameters defined for the simulation. AlO formation is observed in the thin periphery of the fireball where large concentration gradients exist within the first few nanoseconds of the simulation. From pressure and temperature distributions, a strong external shockwave immediately surrounds the high-temperature fireball at these early conditions, where the air behind the shock front that mixes with the fireball is shock-heated up to temperatures of $\approx$2,000 K. Gas-phase polyatomic oxides including AlO_2, Al_2O and Al_2O_2 are also present in the thin chemical reaction zone at the edge of the plasma at these same time delays, although they exist in smaller quantities. The condensation product Al_2O_3 (l) is first observed along the sample surface around a time delay of 30 ns.

As the simulation progresses, the Al plume rapidly expands outwards and interacts with the crater walls. This interaction is believed to partially contribute to initiating vortex formation in the fireball along with other fluid dynamics processes. AlO is pulled into these vortices to react with gas-phase Al to form Al_2O, and by a time delay of 500 ns these species make up the main constituents of the vortices. Over the next several microseconds, aluminum becomes confined in the vortices of the fireball as various molecular species, atomic oxygen, and O_2 are pulled up into the stem (see mass fractions at 5 μs in Fig. 8). Vortex formation was also measured over the same time frame using time-resolved fast-gated imaging, where Al I emission was shown to be concentrated in the plume vortices in Figure 4. As these first vortices continue to lift upwards in the simulation, a second flattened set of vortices is formed towards the sample surface (see mass fractions at 10 μs in Fig. 8). The development of this wider base for the fireball agrees with both fast-gated and shadowgraphic images recorded of the aluminum LA plasma. More specifically, AlO emission was measured to be strongest near the sample surface

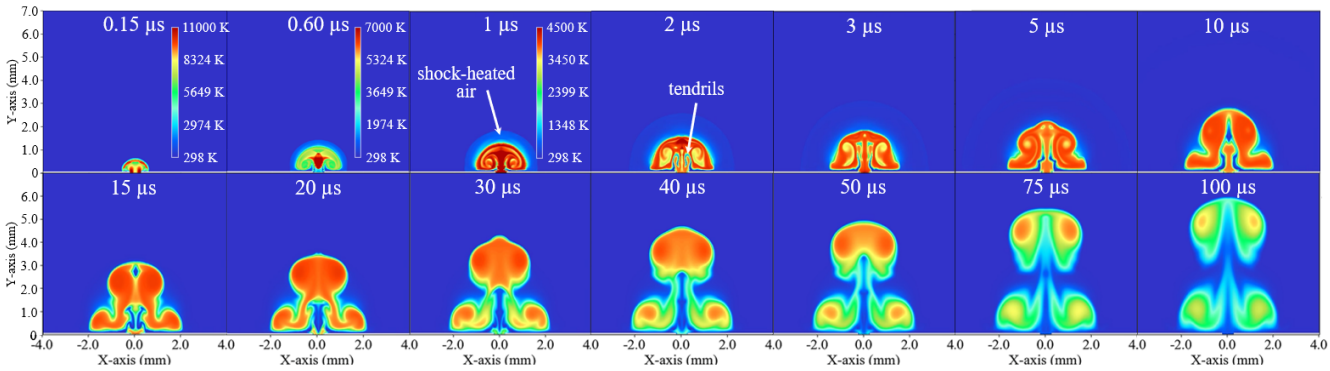

Fig. 7 Temperature evolution of the aluminum fireball predicted by the computational model. The colormap is initially scaled to each individual image due to rapidly changing temperatures and then remains consistent for remaining time frames using the colormap given at 1 µs.

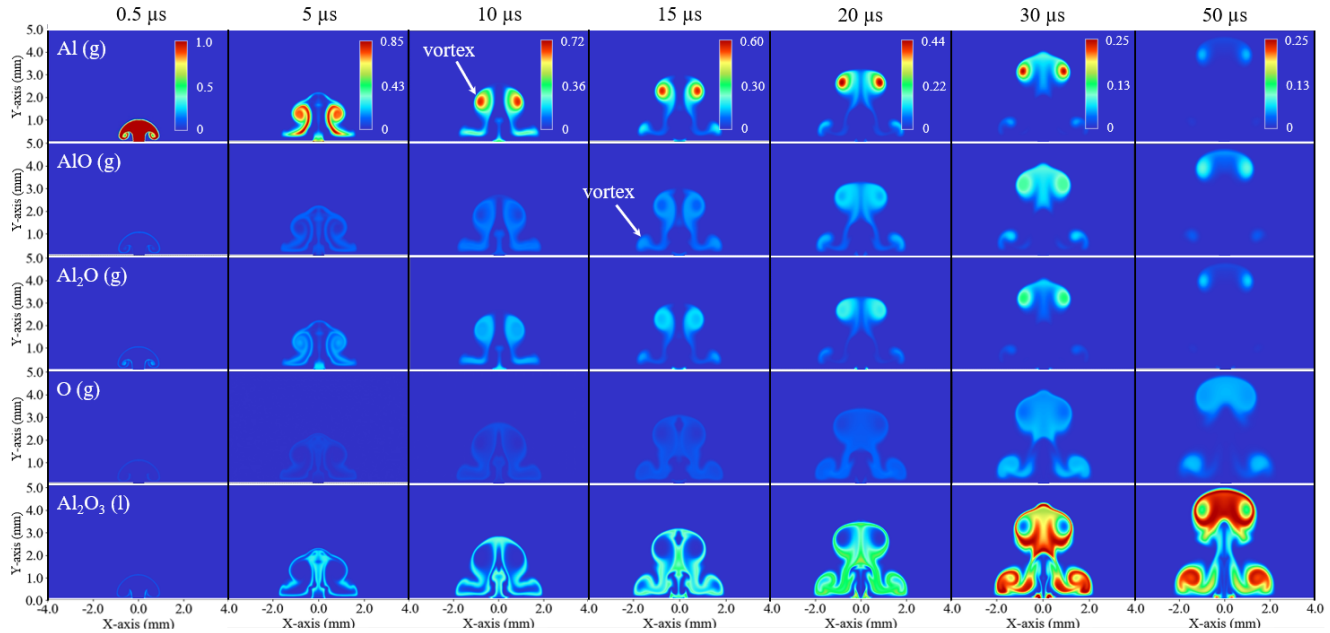

Fig. 8 Selected mass fractions showing temporal evolution of species in the aluminum fireball. The colormaps are scaled by column.

until 30 μs, where molecular emission was shown to combine into a singular structure and move upwards towards the front of the plasma plume (see Fig. 4). The computational model also parallels this behavior, predicting that AlO is preferably located in the head of the fireball by 30 μs. At later time delays, condensed Al_2O_3 (l) is predicted to be the main constituent of the fireball. Small quantities of Al and AlO remain present until 100 μs.

4 Conclusions

The hydrodynamics and shock physics of laser ablation aluminum plasmas has been investigated to explain the impact of plasma-gas intermixing and plasma plume expansion dynamics on chemical reactions in laser-produced plasmas. Experimental measurements in optical spectroscopy and imaging were performed to characterize the transient plasma properties and shock dynamics, where a strong external laser-induced shockwave ($p_1/p_0 = 700$ at 15 ns) was measured to propagate ahead of the rapidly cooling plasma to pre-heat shock-heated air immediately surrounding the plasma plume. AlO was observed to form experimentally as early as 1 μs, while multi-physics simulations predict chemical reactions along the periphery of the expanding plume where temperature gradients are large (thousands of Kelvin) within the first few nanoseconds. The evolving fireball was demonstrated to experience turbulent hydrodynamic processes such as vortex formation, where atomic aluminum became trapped in these vortices as oxygen species were pulled up through the stem to mix and react with aluminum to form AlO and higher polyatomic oxides. The results of this work show that plume hydrodynamics significantly influences the chemical reaction zone morphology and intermixing between reacting species in laser ablation plasmas, while strong shockwaves do not impede the formation of molecular species.

Multi-physics models of the reactive multi-phase flow of laser ablation plasmas provide invaluable and impactful insights into the chemical dynamics of laser ablation plasmas with relevance towards the characterization of optical signatures in oxidizing environments, thin film synthesis using pulsed laser deposition, and debris formation in explosive fireballs. Future work will aim to incorporate ionization processes into the reactive fireball model to investigate laser-induced plasma chemistry subject to various atmospheric conditions.

Conflicts of interest

There are no conflicts to declare.

Acknowledgements

The authors thank the Department of Defense Science, Mathematics, and Research for Transformation (SMART) Scholarship-for-Service Program; Department of Energy National Nuclear Security Administration award number DE-NA0003920; National Science Foundation award number CHE1905301; and Defense Threat Reduction Agency award numbers HDTRA1-20-2-0002 and HDTRA1-19-1-0025 for funding this work.

References

1 Y. Zel'Dovich and Y. Raizer, *Annu. Rev. Fluid Mech.*, 1969, **1**, 385–412.

2 X. Wang, R. Liu, Y. He, Y. Fu, J. Wang, A. Li, X. Guo, M. Wang, W. Guo, T. Zhang, Q. Shu and Y. Yao, *Opt. Express*, 2022, **30**, 4718–4736.

3 C. Kimblin, R. Trainham, G. A. Capelle, X. Mao and R. E. Russo, *AIP Adv.*, 2017, **7**, 095208.

4 M. Burton, A. Auner, J. Crowhurst, P. Boone, L. Finney, D. Weisz, B. Koroglu, I. Jovanovic, H. Radousky and K. Knight, *Sci. Rep.*, 2022, **12**, 4030.

5 E. Kautz, P. Skrodzki, M. Burger, B. Bernacki, I. Jovanovic, M. Phillips and S. Harilal, *J. Anal. At. Spectrom.*, 2019, **34**, 2236.

6 E. Weerakkody, D. Weisz, J. Crowhurst, B. Koroglu, T. Rose, H. Radousky, R. Stillwell, J. Jeffries and N. Glumac, *Spectrochim. Acta B: At. Spectrosc*, 2020, **170**, 105925.

7 A. Botto, B. Campanella, S. Legnaioli, M. Lezzerini, G. Lorenzetti, S. Pagnotta, F. Poggialini and V. Palleschi, *J. Anal. At. Spectrom.*, 2019, **34**, 81–103.

8 V. Lazic, F. Colao, R. Fantoni and V. Spizzichino, *Spectrochim. Acta B: At. Spectrosc.*, 2005, **60**, 1014–1024.

9 B. Busser, S. Moncayo, J.-L. Coll, L. Sancey and V. Motto-Ros, *Coord. Chem. Rev.*, 2018, **358**, 70–79.

10 O. Samek, D. C. Beddows, H. H. Telle, J. Kaiser, M. Liska, J. O. Caceres and A. G. Urena, *Spectrochim. Acta B: At. Spectrosc.*, 2001, **56**, 865–875.

11 C. Fabre, *Spectrochim. Acta B: At. Spectrosc.*, 2020, **166**, 105799.

12 J. M. Anzano, M. A. Villoria, A. Ruiz-Medina and R. J. Lasheras, *Anal. Chim. Acta*, 2006, **575**, 230–235.

13 M. Z. Martin, N. Labbe, N. Andre, R. Harris, M. Ebinger, S. D. Wullschleger and A. A. Vass, *Spectrochim. Acta B: At. Spectrosc.*, 2007, **62**, 1426–1432.

14 C. M. Bridge, J. Powell, K. L. Steele and M. E. Sigman, *Spectrochim. Acta B: At. Spectrosc.*, 2007, **62**, 1419–1425.

15 S. S. Harilal, B. Brumfield, N. LaHaye, K. Hartig and M. Phillips, *Appl. Phys. Rev.*, 2018, **5**, 021301.

16 M. Burger, L. Finney, L. Garrett, S. Harilal, K. Hartig, J. Nees, P. Skrodzki, X. Xiao and I. Jovanovic, *Spectrochim. Acta B: At. Spectrosc.*, 2021, **179**, 106095.

17 G. C.-Y. Chan, L. R. Martin, L. D. Trowbridge, Z. Zhu, X. Mao and R. E. Russo, *Spectrochim. Acta B: At. Spectrosc.*, 2021, **176**, 106036.

18 S. M. Clegg, R. Wiens, A. K. Misra, S. K. Sharma, J. Lambert, S. Bender, R. Newell, K. Nowak-Lovato, S. Smrekar, M. D. Dyar and S. Maurice, *Appl. Spectrosc.*, 2014, **68**, 925–936.

19 S. Schröder, K. Rammelkamp, F. Hanke, I. Weber, D. S. Vogt, S. Frohmann, S. Kubitza, U. Böttger and H. Hübers, *J. Raman Spectrosc.*, 2019, **51**, 1667–1681.

20 R. E. Russo, T. W. Suen, A. A. Bol'shakov, J. Yoo, O. Sorkhabi, X. Mao, J. Gonzalez, D. Oropezaa and V. Zorba, *J. Anal. At. Spectrom.*, 2011, **26**, 1596–1603.

21 E. J. Kautz, M. C. Phillips, A. Zelenyuk and S. S. Harilal, *Phys. Plasmas*, 2022, **29**, 053509.

22 K. C. Hartig, S. S. Harilal, M. C. Phillips, B. E. Brumfield and I. Jovanovic, *Opt. Express*, 2017, **25**, 11477–11490.

23 K. C. Hartig, I. Ghebregziabher and I. Jovanovic, *Sci. Rep.*, 2017, **7**, 43852.

24 E. H. Kwapis, E. Villa-Aleman and K. C. Hartig, *Spectrochimica Acta Part B: Atomic Spectroscopy*, 2023, **200**, 106610.

25 M. Butterfield, T. Durakiewicz, E. Guziewicz, J. Joyce, A. Arko, K. Graham, D. Moore and L. Morales, *Surf. Sci.*, 2004, **571**, 74–82.

26 F. R. Doucet, P. J. Faustino, M. Sabsabi and R. C. Lyon, *J. Anal. At. Spectrom.*, 2008, **23**, 694–701.

27 J. Li, Z. Yu, Z. Du, Y. Ji and C. Liu, *Remote Sens.*, 2022, **12**, 2771.

28 N. Melikechi, R. Wiens, H. Newsom and S. Maurice, *Optics & Photonics News*, 2013, **24**, 26–33.

29 D. H. Lowndes, D. Geohegan, A. Puretzky, D. Norton and C. Rouleau, *Science*, 1996, **273**, 898–903.

30 K. Hartig, B. Brumfield, M. Phillips and S. Harilal, *Spectrochim. Acta B: At. Spectrosc.*, 2017, **135**, 54–62.

31 P. Skrodzki, M. Burger, I. Jovanovic, M. Phillips, J. Yeak, B. Brumfield and S. Harilal, *Phys. Plasmas*, 2019, **26**, 083508.

32 A. D. Giacomo and J. Hermann, *J. Phys. D: Appl. Phys.*, 2017, **50**, 183002.

33 D. Weisz, J. Crowhurst, M. Finko, T. Rose, B. Koroglu, R. Trappitsch, H. Radousky, W. Siekhaus, M. Armstrong, B. Isselhardt, M. Azer and D. Curreli, *J. Phys. Chem. A*, 2018, **122**, 1584–1591.

34 E. R. Wainwright, S. W. Dean, F. C. D. L. Jr., T. P. Weihs and J. L. Gottfried, *Appl. Phys. A*, 2020, **126**, 83.

35 S. Harilal, B. Brumfield, B. Cannon and M. Phillips, *Anal. Chem.*, 2016, **88**, 2296–2302.

36 S. Shabanov and I. Gornushkin, *Appl. Phys. A*, 2015, **121**, 1087–1107.

37 J. Hermann, A. Lorusso, A. Perrone, F. Strafella, C. Dutouquet and B. Torralba, *Phys. Rev. E*, 2015, **92**, 053103.

38 T. Itina, J. Hermann, P. Delaporte and M. Sentis, *Phys. Rev. E*, 2002, **66**, 066406.

39 S. Shabanov and I. Gornushkin, *Spectrochim. Acta B: At. Spectrosc*, 2014, **100**, 147–172.

40 S. Aggoune, F. Vidal and E. Amara, *Appl. Phys. A*, 2010, **101**, 167–171.

41 M. Capitelli, A. Casavola, G. Colonna and A. D. Giacomo, *Spectrochim. Acta B: At. Spectrosc*, 2004, **59**, 271–289.

42 S. Irimiciuc, I. Mihăilă and M. Agop, *Phys. Plasmas*, 2014, **21**, 093509.

43 S. Harilal, G. Miloshevsky, P. Diwakar, N. LaHaye and A. Hassanein, *Phys. Plasmas*, 2012, **19**, 083504.

44 E. R. Wainwright, C. J. Miller, L. Giri, R. A. Pesce-Rodriguez, C.-C. Wu and J. L. Gottfried, *Spectrochim. Acta B: At. Spectrosc*, 2023, **199**, 106597.

45 R. W. Houim, Technical Report AFRL-AFOSR-VA-TR-2020-0021, Air Force Research Laboratory, AF Office of Scientific Research, Arlington, VA, 2020.

46 D. R. Guildenbecher, A. R. Dallman, E. M. Hall, B. R. Halls, E. M. Jones, S. P. Kearney, R. T. Marinis, C. Murzyn, D. R. Richardson, F. Perez, P. L. Reu, A. D. Thompson, M. C. Welliver, E. C. Mazumdar, T. L. Pourpoint, C. M. White, A. D. Brown, S. Balachandar and R. W. Houim, Technical Report SNL/SAND2020-9893, U.S. Department of Energy, Sandia National Laboratory, Albuquerque, NM, 2020.

47 S. Guhathakurta and R. W. Houim, *J. Loss Prev. Process Ind.*, 2021, **72**, 104509.

48 J. W. Posey, B. Roque, S. Guhathakurta and R. W. Houim, *Phys. Fluids*, 2021, **33**, 113308.

49 R. W. Houim, A. Ozgen and E. S. Oran, *Combust. Theor. Model.*, 2016, **20**, 1068–1087.

50 R. W. Houim and B. D. Taylor, *Proc. Combust. Inst.*, 2019, **37**, 3513–3520.

51 S. Heiroth, J. Koch, T. Lippert, A. Wokaun, D. Günther, F. Garrelie and M. Guillermin, *J. Appl. Phys.*, 2010, **107**, 014908.

52 J. M.W. Chase, C. Davies, J. J.R. Downey, D. Frurip, R. McDonald and A. Syverud, *J. Phys. Chem. Ref. Data*, 1985, **14**, Suppl. 1.

53 B. McBride, S. Gordon and M. Reno, *Coefficients for calculating thermodynamic and transport properties of individual species, NASA Technical Memorandum 4513*, 1993.

54 A. M. Starik, P. S. Kuleshov, A. S. Sharipov, N. S. Titova and C.-J. Tsai, *Combust. Flame*, 2014, **161**, 1659–1667.

55 C. Johnston and A. Brandis, *JQSRT*, 2014, **149**, 303–317.

56 M. Hobbs and M. Baer, *Shock Waves*, 1992, **2**, 177–187.

57 R. W. Houim and K. K. Kuo, *J. Comput. Phys.*, 2011, **230**, 8527–8553.

58 R. Houim and E. Oran, *J. Fluid Mech.*, 2016, **789**, 166–220.

59 R. Houim, *Shock Waves*, 2021, **31**, 851–875.

60 A. E. Sherbini, T. E. Sherbini, H. Hegazy, G. Cristoforetti, S. Legnaioli, V. Palleschi, L. Pardini, A. Salvetti and E. Tognoni, *Spectrochim. Acta B: At. Spectrosc*, 2005, **60**, 1573–1579.

61 E. Oks, *Stark Broadening of Hydrogen and Hydrogenlike Spectral Lines in Plasmas*, Alpha Science International, 1st edn, 2006.

62 H. Griem, *Plasma Spectroscopy*, McGraw-Hill Book Company, 1964.

63 C. Western, *J. Quant. Spectrosc. Radiat. Transfer*, 2017, **186**, 221–242.

64 O. Launila and L. Berg, *J. Molec. Spectros.*, 2011, **265**, 10–14.

65 M. Saksena, M. Deo, K. Sunanda, S. Behere and C. Londhe, *J. Molec. Spectros.*, 2008, **247**, 47–56.

66 X. Bai and T. C. Steimle, *ApJ.*, 2020, **889**, 147.

67 G. Hérbert, R. Nicholls and C. Linton, *J. Quant Spectrosc, Radiat. Transfer*, 1980, **23**, 229–235.

68 R. Kurucz and B. Bell, *Atomic Line Data Kurucz CD-ROM No. 23. Smithsonian Astrophysical Observatory*, 1995.

69 K. K. Herrera, E. Tognoni, N. Omenetto, B. W. Smith and J. D. Winefordner, *J. Anal. At. Spectrom.*, 2009, **24**, 413–425.

70 D. M. Surmick and C. G. Parigger, *Appl. Spectrosc.*, 2014, **68**, 992–996.

71 D. M. Surmick and C. G. Parigger, *J. Phys.: Conf. Ser.*, 2014, **548**, 012046.

72 E. H. Kwapis, M. Hewitt and K. C. Hartig, *Opt. Express*, 2023,

31, 10694–10708.

73 K. Shimamura, J. A. Ofosu, K. Komurasaki and H. Koizumi, *Jpn. J. Appl. Phys.*, 2015, **54**, 016201.

74 J. L. Gottfried, *Phys. Chem. Chem. Phys.*, 2014, **16**, 21452–21466.

75 N. Arnold, J. Gruber and J. Heitz, *Appl. Phys. A*, 1999, **69**, S87–S93.

76 S.-B. Wen, X. Mao, R. Greif and R. E. Russo, *J. Appl. Phys.*, 2007, **101**, 023114.

77 S. Courtiaud, N. Lecysyn, G. Damamme, T. Poinsot and L. Selle, *Shock Waves*, 2019, **29**, 339–353.

78 G. Callies, P. Berger and H. Hugel, *J. Phys. D: Appl. Phys.*, 1995, **28**, 794–806.

79 Y. Zhang, Y. Ito, H. Sun and N. Sugita, *Opt. Express*, 2022, **30**, 37394–37406.